CORA Cork Open Research Archive
Cartlann Taighde Oscailte Chorcaí

Title	Hydrogenated silicon nanoclusters with a permanent electric dipole moment for the controlled assembly of silicon-based nanostructures
Authors	Jardali, Fatme;Keary, Bryan P.;Perrotin, Tatiana;Silva, François;Vanel, Jean-Charles;Bonnassieux, Yvan;Mazouffre, Stéphane;Ruth, Albert A.;Leulmi, Mohamed E.;Vach, Holger
Publication date	2021-11-16
Original Citation	Jardali, F., Keary, B. P., Perrotin, T., Silva, F., Vanel, J.-C., Bonnassieux, Y., Mazouffre, S., Ruth, A. A., Leulmi, M. E. and Vach, H. (2021) 'Hydrogenated silicon nanoclusters with a permanent electric dipole moment for the controlled assembly of silicon-based nanostructures', ACS Applied Nano Materials, 4(11), pp.12250-12260. https://doi.org/10.1021/acsanm.1c02754
Type of publication	Article (peer-reviewed)
Link to publisher's version	10.1021/acsanm.1c02754
Rights	© 2021, Association for Computing Machinery. This is the author's version of the work. It is posted here for your personal use. Not for redistribution. The definitive Version of Record was published in ACS Applied Nano Materials: https://doi.org/10.1021/acsanm.1c02754
Download date	2026-11-16 09:45:29
Item downloaded from	https://hdl.handle.net/10468/12268

UCC
University College Cork, Ireland
Coláiste na hOllscoile Corcaigh

Supporting Information: Hydrogenated Silicon Nanoclusters with a Permanent Electric Dipole Moment for the Controlled Assembly of Silicon-Based Nanostructures

Fatme Jardali,[†] Bryan Patrick Keary,[‡] Tatiana Perrotin,[¶] François Silva,[†] Jean-Charles Vanel,[†] Yvan Bonnassieux,[†] Stéphane Mazouffre,[¶] Albert A. Ruth,[‡] Mohamed E. Leulmi,[§] and Holger Vach[*,†,‖]

†*LPICM, CNRS, Ecole Polytechnique, IP Paris, Palaiseau, France*

‡*Physics Department / Environmental Research Institute, University College Cork, Cork, Ireland*

¶*ICARE, CNRS, Orléans, France*

§*Center for SiNC Applications, Paris, France*

‖*Centre for Research in Molecular Modeling, Concordia University, Montreal, Canada*

E-mail: holger.vach@polytechnique.edu

Life stages of dust particles

The dust particle formation and growth in a low-pressure RF discharge is divided into a three-stage process.[1] An illustration of the growth process is given in Fig. S1 where the first two columns correspond to the first stage:

1. Formation and accumulation phase, *i.e.* a conversion process from gas species to particles. This process is stimulated by the fast silane molecule and radical interactions with negative ion clusters. The first nucleus for the formation of dust nanoparticles is SiH_3^-. In the early stages of their formation, the fraction of charged nanoclusters is less than 1‰. At this size scale, they cannot carry more than one elementary charge and experience charge fluctuations. Therefore, the quasi-neutrality of the plasma is strictly respected.[2,3] The size of those first-generation particles is about 2 nm. When the concentration of those particles increases up to a critical value of 10^{10} - 10^{11} cm^{-3}, which corresponds to a mean distance between the nanoparticles of about 1 μm, the new-particle formation terminates.

2. Agglomeration phase. A fast agglomeration process takes place leading to large (50 nm) dust particles.

3. Further growth of the dust particles takes place by the attachment of radicals on their surface until micrometer sized dust particles are obtained.

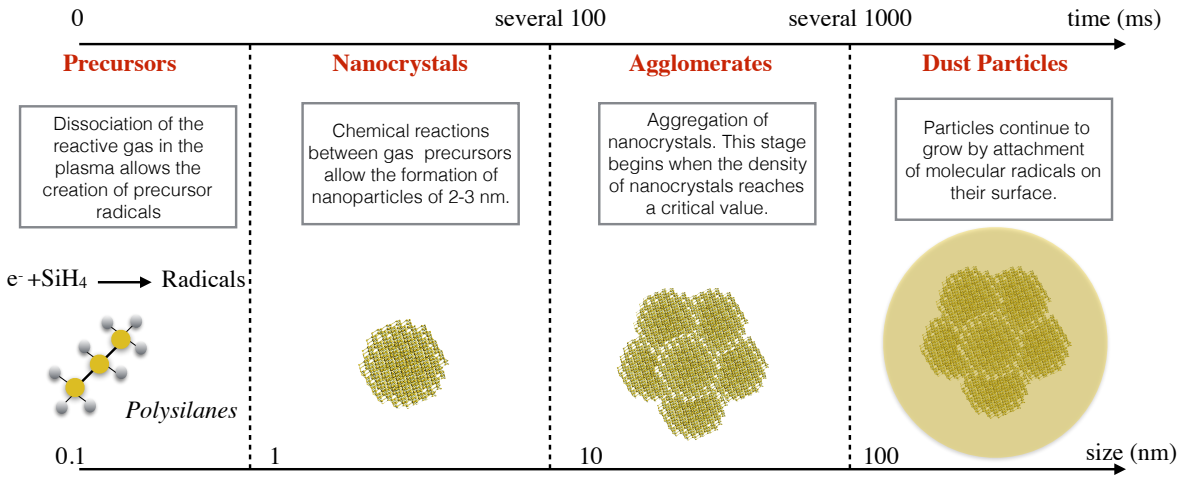


Fig. S 1. Different stages of the growth of dust particles in a plasma reactor.

Short history of non-tetrahedral, ultrastable, and aromatic-like silicon nano clusters (SiNCs)

Theoretical investigations on the kinetics of SiNC nucleation and growth during the first phase of the growth process brought to the fore the generation of 1 nm sized SiNCs with a new allotropic form of silicon.[4,5] Studies revealed that in a plasma enhanced chemical vapor deposition (PECVD) reactor under appropriate experimental conditions, the growth of SiNCs can be steered toward surprisingly stable structures that are much more stable than all previously known silicon clusters.[5–11] While some of the pioneer model clusters, as $Si_{19}H_{12}$ and $Si_{21}H_{12}$, both with high-symmetry structures, were already found to be more stable than the well-known silicon fullerene $Si_{20}H_{20}$,[5,10] recent simulations showed that a low-symmetry $Si_{19}H_{12}$ isomer can even be 5.4 eV more stable than its high-symmetry counterpart.[11] Those

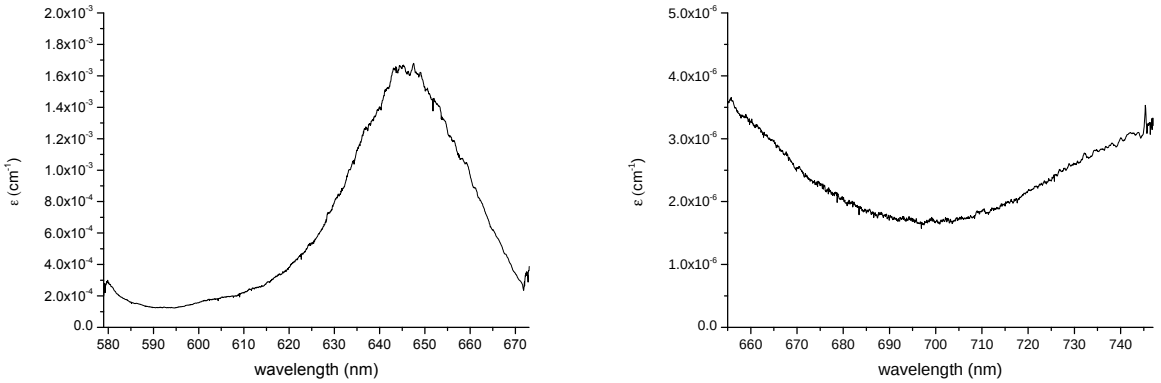
ultrastable SiNCs form spontaneously by self-assembly, exhibit no tetrahedral structures and can either be highly symmetric or completely irregular. Nearly independent of their precise stoichiometry and size of around 1 nm, they are always found to have at least one over-coordinated Si atom. As a result of this over-coordination, the SiNCs possess electron-deficient bonds, which induce efficient electron delocalization between the over-coordinated Si atom and its neighbors, resulting in a higher stability than the one of previously known tetrahedral silicon clusters, for which the electrons can be viewed as being perfectly localized between Si atoms.[9,12]

We would like to remind here that we do not define "ultrastability" for a given cluster based on a certain threshold value for its binding energy; but simply on the fact that electron delocalization plays a significant role for its stability; *i.e.*, we use the term "ultrastability" in a comparable manner as the term "extra-stability" in the classical multi-bond aromaticity concept for conjugated systems without limiting ourselves to connected p orbitals.[12] As a result of the over-coordination and the highly delocalized nature of the electrons, those 1 nm non-tetrahedral and ultrastable SiNCs exhibit aromatic-like properties, such as extremely high magnetically induced ring currents of about 42.0 $\mathrm{nAT^{-1}}$ for nanoclusters with $Si_{19}H_{12}$ stoichiometry,[9] while the corresponding value for the most famous aromatic molecule benzene is only 12.9 $\mathrm{nAT^{-1}}$. Most importantly, theoretical studies have revealed that, (i) the non-centered over-coordinated Si atom bears a permanent charge, giving the SiNCs a strong permanent electrical dipole moment, and that (ii) their optical absorption extends from the ultraviolet through the visible until the infrared spectral region.[8,10,13] Without this new nano-silicon allotrope, the spectral absorption of standard tetrahedral and pure hydrogenated SiNCs of this size is limited to the ultraviolet frequency range. To extend the response to the visible and infrared region, expensive and/or toxic metal atoms are often incorporated in tetrahedral SiNCs. Therefore, the substantially red-shifted spectral response of non-tetrahedral plasma-born aromatic-like SiNCs might readily lead to the environmentally friendly replacement of expensive or toxic nanoclusters. Consequently, they can be applied in

various fields of research reaching from potential cancer treatment to photovoltaic devices.[9,13]

Measured absorption spectra of plasma-born SiNCs

In Fig. S2, we show the measured absorption (units of cm^{-1}) of the plasma-born SiNCs, obtained according to equation (1) in the main text using two sets of mirrors covering two regions in the visible-infrared spectral range; set 1: 575 - 665 nm (see Fig. S2a) and set 2: 655 - 745 nm (see Fig. S2b). The light intensities transmitted through the cavity with and without plasma were measured for a gas pressure of 0.115 mbar and a temperature of 150 °C. The plasma on-time was 2 s and the gate delay time (the time between the end of the RF pulse and the beginning of the acquisition measurement) was set to 100 ms. Under these experimental conditions and for the given synchronisation parameters, the maximum size of SiNCs created in the plasma is $\sim$ 1 nm; this claim has also been confirmed by our AFM measurements shown in Figs. 4c and 4e. The spectra of these SiNCs were averaged over long times (1000 acquisitions). As can be seen from Fig. S2a, the spectrum shows a strong absorption peak in the visible region around 645 nm; then, the signal decreases until around 670 nm. In Fig. S2b, the spectrum looks coherent with respect to the spectrum in Fig. S2a, *i.e.*, the signal in the latter has a maximum around 645 nm and then decreases until 670 nm, while the signal in the former spectrum decreases from its beginning at about 655 nm until 700 nm and then increases again.



(a) **(b)**

Fig. S 2. Measured absorption spectra of plasma-born SiNCs of size ∼1 nm using two sets of high-reflectivity mirrors. Absorption spectrum measured using the set of mirrors covering a spectral range of 575 - 665 nm (set 1) in **a**, and 655 - 745 nm (set 2) in **b**. Experimental conditions: Plasma on-time is 2 s. Gas pressure is 0.115 mbar. Gas temperature and gas mixture flow rate are 150 °C and 10 sccm, respectively. Gate width is set to 10 ms. Gate delay is set to to 100 ms.

Measured absorption spectra of plasma-born SiNCs with different gate delay times

In Fig. S3, we show a set of absorption measurements that were performed with different gate delay times, between 1 ms and 250 ms, using mirror set 1. The measurements were performed with similar experimental conditions as before, but with a gas pressure of 0.165 mbar. The spectra were averaged over 150 acquisitions. We notice that the intensity of the measured absorption varies with the delay time. The absorption increases with the increase in delay time until 150 ms and then rapidly decreases. This can be explained as follows: when we turn off the plasma, the absorbing SiNCs, mainly located above the detection beam with the highest density near the shower head, move downwards with the gas flow. They cross the detection beam after a few milliseconds, with a maximum density of SiNCs reaching the light beam at 150 ms. Waiting for a longer time (200 ms), we find a drop in the absorption

indicating that most of the absorbing SiNCs had already crossed the detection beam.

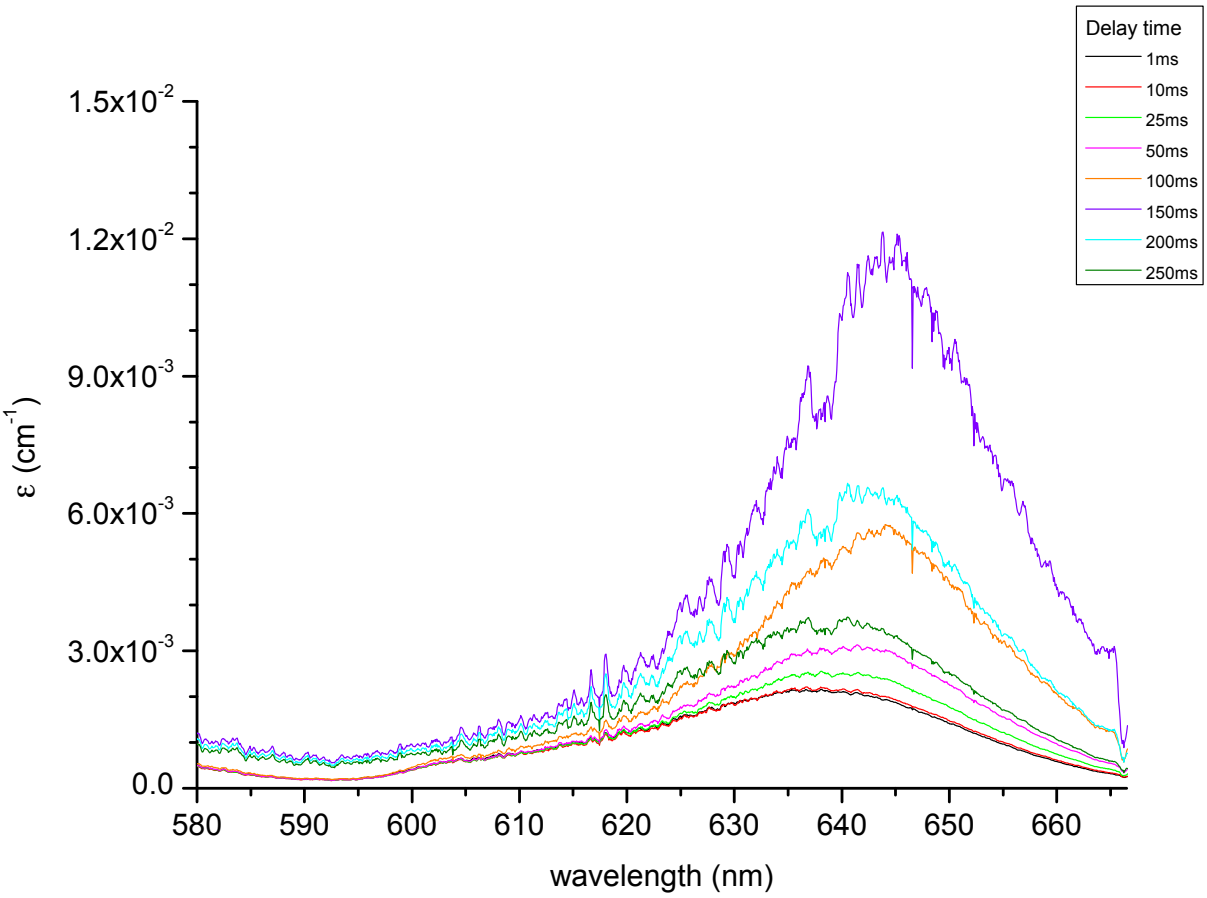


Fig. S 3. Measured absorption spectra of plasma-born SiNCs of size ∼1 nm with different gate delay times. Experimental conditions: Plasma on-time is 2 s. Gas pressure is 0.165 mbar. Gas temperature and flow rate are 150 °C and 10 sccm, respectively. Gate width is 10 ms.

Measured absorption spectra of plasma-born SiNCs with a range of plasma times

In Fig. S4 we present a set of measurements performed for different plasma times, *i.e.* for different sizes of SiNCs, with a gas pressure of 0.065 mbar and a gate delay time of 50 ms. Since under the experimental conditions we used, the SiNCs start to agglomerate after about 6 s, when the particles have a size of about 2 nm (*i.e.* ∼ 200 Si atoms), we can roughly

estimate that at a plasma pulse of 2 s, the SiNC consist of $\sim$ 70 Si atoms and have an approximate size of 1.4 nm. Therefore, the change in the size of the SiNCs between 6 s and 2 s is approximately a factor of 1.4. If the measured extinction corresponded to scattering and not absorption, the change in the intensity of the signal would vary by 1.4^6, *i.e.* by 7.5. However, the spectra clearly show that the ratio of intensities between 6 s and 2 s (purple and green lines in Fig. 4) is only 1.4. This confirms our prior assumption that the measurements performed on SiNCs of this size correspond to absorption and not scattering.

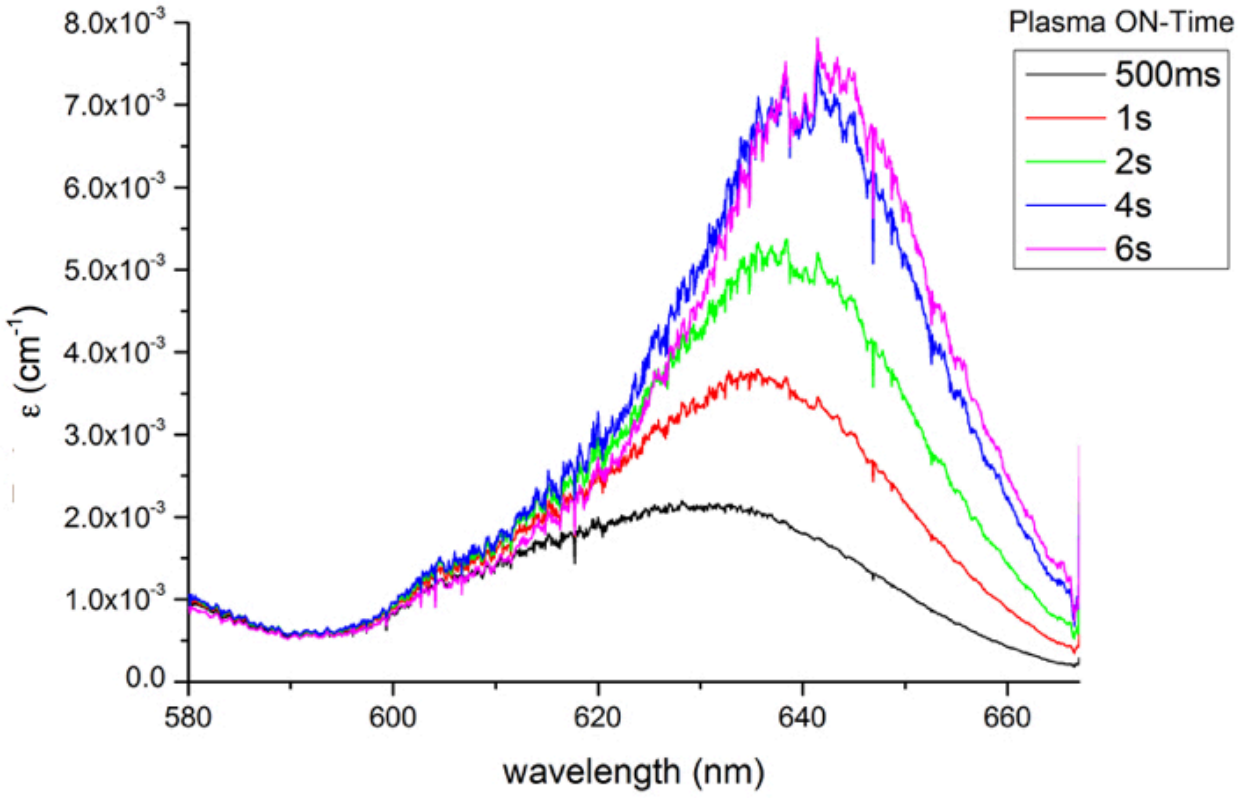


Fig. S 4. Measured absorption spectra of plasma-born SiNCs with different plasma times. Experimental conditions: Gas pressure is 0.065 mbar. Gas temperature and flow rate are 150 °C and 10 sccm, respectively. Gate width is 10 ms and gate delay is 50 ms.

Schematic representation of the reactor chamber

Fig. S5 shows a cross-sectional view of the designed reactor chamber taking into account its exact configuration and dimensions. Thick blue lines indicate the lines along which we

calculated the different components of the electric field; L is a horizontal axis that, to a good approximation, represents the axis of the light beam, L_1 to L_{12} are several vertical axes taken from the top to the bottom electrode with lengths of 40 mm. The dipole forces were then calculated from the gradients of the electric fields.

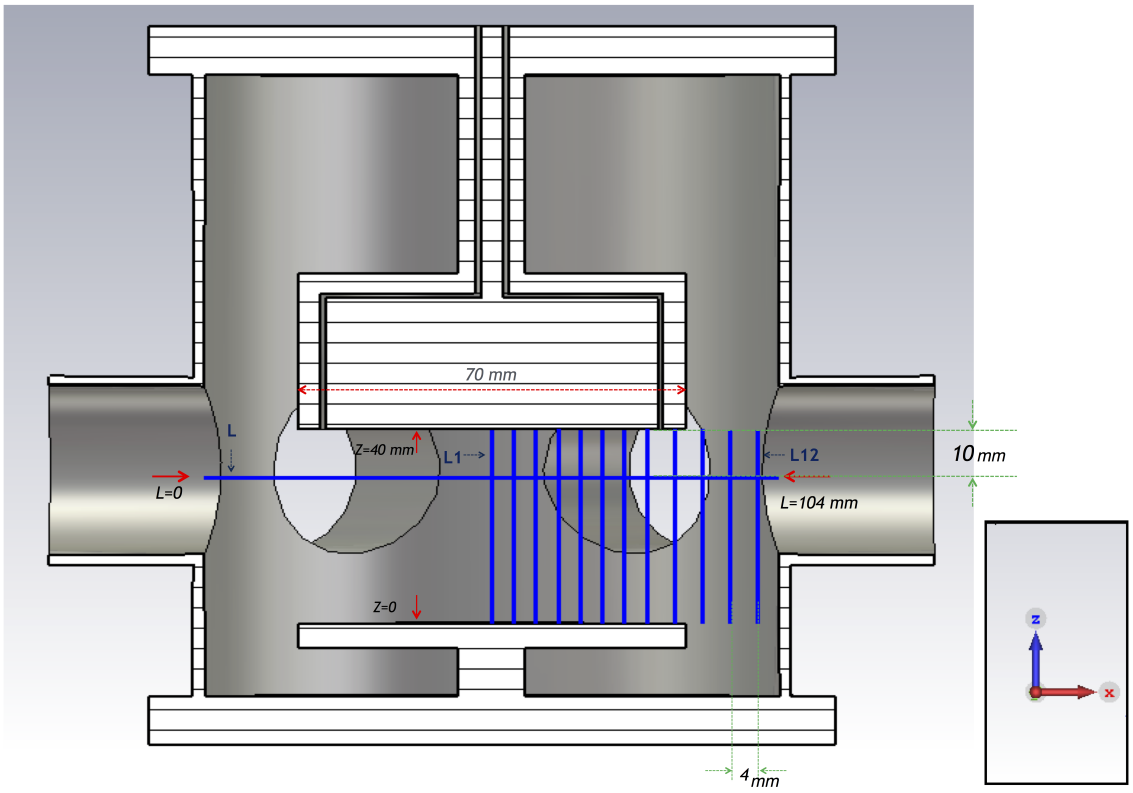


Fig. S 5. A schematic representation of the reactor chamber. L and L_n indicate the lines along which the simulations of the electric field were taken into consideration in our analysis: x-component of the electric field through the light beam along L, z-component of the electric field from the top to the bottom electrode along L_1 until L_{12}.

Dipole forces acting on the SiNCs along the z-axis

In the following, we track the behavior of nanoclusters, under the influence of the dipole forces after the plasma is switched off. In Fig. S5, the lines along which we calculated the

different components of the electric field are shown as thick blue lines. The dipole forces were calculated from the gradients of the electric fields. In order to simplify the analysis, we distinguish between the dipole forces acting on the SiNCs in the z-direction and those in the plane of the light beam. Since the reactor chamber has a cylindrical geometry, we performed the analysis using cylindrical coordinates (r, θ, z). To this end, we calculated the non-zero components of the electric field ((E_r) and (E_z)) from which we found the gradients and the corresponding dipole forces. Fig. S6 shows the dipole forces calculated along the different lines L_2 to L_{12} (see Fig. S5); *i.e.* the dipole force acting on the SiNCs in the z-direction, with an applied bias of 240 V and assuming that the SiNCs possess a dipole moment of 2 Debye, in agreement with the theoretically predicted permanent dipole moment. We notice from Fig. S6a that the dipole forces in the region of interest (between the top electrode and the light beam, *i.e.* between 30 and 40 mm, are negative for lines L_1 to L_8, *i.e.* the forces are directed downward toward the light beam. While Figs. S6b and c show that the dipole forces become mainly positive in this region for lines L_9 to L_{12}. Nevertheless, comparing the strength of the dipole forces with the neutral drag force acting on $\sim$1 nm nanoclusters in the z-direction,[14] we find that the calculated dipole forces are about four orders of magnitude weaker. Moreover, all other forces acting on the nanoclusters, such as the gravitational force and the thermophoretic force, can be neglected in our case due to the very small size of the SiNCs and the absence of a significant temperature gradient in the reactor, respectively. Therefore, we conclude that the movement of the SiNCs in the z-direction is mostly determined by the neutral drag force. Consequently, SiNCs initially located in the same horizontal plane will reach the light beam at the same time.

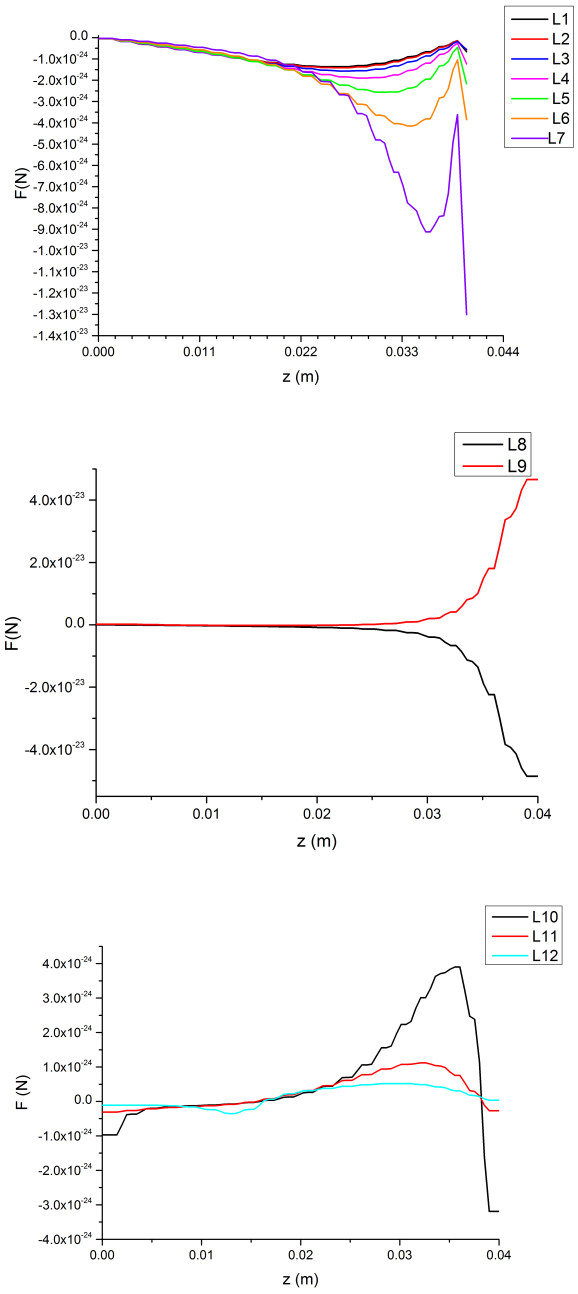


Fig. S 6. Dipole forces acting on the nanoclusters in the z-direction. The dipole forces are calculated for an applied DC bias of 240 V, assuming that the nanoclusters possess a permanent dipole moment of 2 Debye.

Particle density distributions from trajectories simulations

At the instant the plasma is switched off, the SiNCs lose their negative charges to the positively charged argon ions. At this moment, they are mainly equally distributed in a region under the powered electrode and start moving down toward the detection plane due to the gas flow in the reactor. In the absence of any applied DC bias or without any permanent electric dipole moment, the SiNCs would approximately keep their initial density distribution.[15] However, in the presence of a DC bias and a permanent electric dipole moment, the SiNCs start spreading out radially as they move downward. In order to gain a deeper insight into the density of the SiNCs as they move to the detection beam plane, we simulated their trajectories starting from their initial positions in a region below the top electrode until they reach the light beam where they are detected. To this end, the density of particles as function of their radial position (measured from the center of the electrode) was calculated at given parallel planes in the z-direction.

Short movie illustrating the silicon nanowire growth

The attached movie shows the arrival of a fourth SiNC approaching a small silicon nanowire already formed as the result of the prior, sequential arrival of three other SiNCs. To this end, ab initio calculations were performed by using DFT within the generalized gradient approximation including van der Waals corrections as implemented in the Vienna simulation package (VASP).[16,17] The Perdew-Burke-Ernzerhof functional[18] with the van der Waals-D2 correction[19] was used to describe the exchange-correlation interaction. The core electrons were described by the projector-augmented wave method.[20] The plane-wave basis set was restricted to a cutoff energy of 500 eV. The LaB_6 substrate was modeled using periodic boundary conditions in the x and y directions, keeping the bottom layer fixed. The vacuum

region is as thick as 10.0 nm. The convergence criterion of total energy for self-consistent field calculations was chosen to be 10^{-4} eV. The shown *ab initio* molecular dynamics (AIMD) simulations were performed within the NVT ensemble[21] using the Nose-Hoover thermostat[22] for temperature control. While the present simulation was started at an initial distance of 3nm between the fourth and the third SiNCs, we only show the last moments of arrival when a covalent bond between the two SiNCs was formed in the movie. Please, note that the AIMD simulation was performed at the experimental temperature of 150°C. Therefore, not all covalent bonds are displayed as connecting lines all the time because the interatomic distances periodically become longer than those at zero Kelvin.

Thermionic electron emission

The relationship between the electron current density J_0 and the work function (WF) ϕ_0 of a material at a temperature T is given by Richardson-Dushman's law:[23–26]

$$J_0 = A_G T^2 \exp\left(\frac{-e\phi_0}{k_B T}\right) \tag{1}$$

where T is the temperature in Kelvin, e the elementary charge, k_B the Boltzmann constant, ϕ_0 the work function (WF) in eV and A_G the Dushman constant that can be expressed as A_G=λ_R A_0 with λ_R being a material-specific correction factor that is typically of the order of 0.5, and A_0 is a universal constant:

$$A_0 = \frac{4\pi m_e k_B^2 e}{h^3} \tag{2}$$

m_e is the electron mass and h the Planck constant. Thus A_0 = 120.4 A.cm^{-2}.K^{-2}.

The Schottky effect describes the reduction of the WF of the material due to the presence of an electric field at its emitting surface. In our case this electric field is related to the potential difference between the emitting element and the surface of the collecting anode.

The modified WF is given by

$$\phi = \phi_0 - \sqrt{\frac{e^3 E}{4\pi\epsilon_0}} \tag{3}$$

E is the electric field and ϵ_0 is the vacuum permittivity. The Richardson-Dushman equation can be written when taking into account the Schottky effect [26] as:

$$J = A_0 T^2 \exp\left(\frac{-e\phi}{k_B T}\right) = A_0 T^2 \exp\left(\frac{-e\phi_0}{k_B T}\right) \exp\left(\frac{\sqrt{\frac{e^3 E}{4\pi\epsilon_0}}}{k_B T}\right) = J_0 \exp\left(\frac{\sqrt{\frac{e^3 E}{4\pi\epsilon_0}}}{k_B T}\right) \tag{4}$$

The WF can be deduced from this equation that can be linearised by taking its logarithm:

$$\ln(J) = \ln(J_0) + \left(\frac{\sqrt{\frac{e^3}{4\pi\epsilon_0}}}{k_B T}\right) \sqrt{E} = \ln(J_0) + \left(\frac{C}{T}\right) \sqrt{V} \tag{5}$$

where C is a constant. We assume here that the electric field is homogeneous between the emitting surface and the anode that is located at a distance d apart and given by $E = V/d$ with V being the potential difference between them. Thus, for a given constant temperature of the emitting surface, the logarithm of the current density will linearly vary with the root mean square of the potential (see Fig. 7).

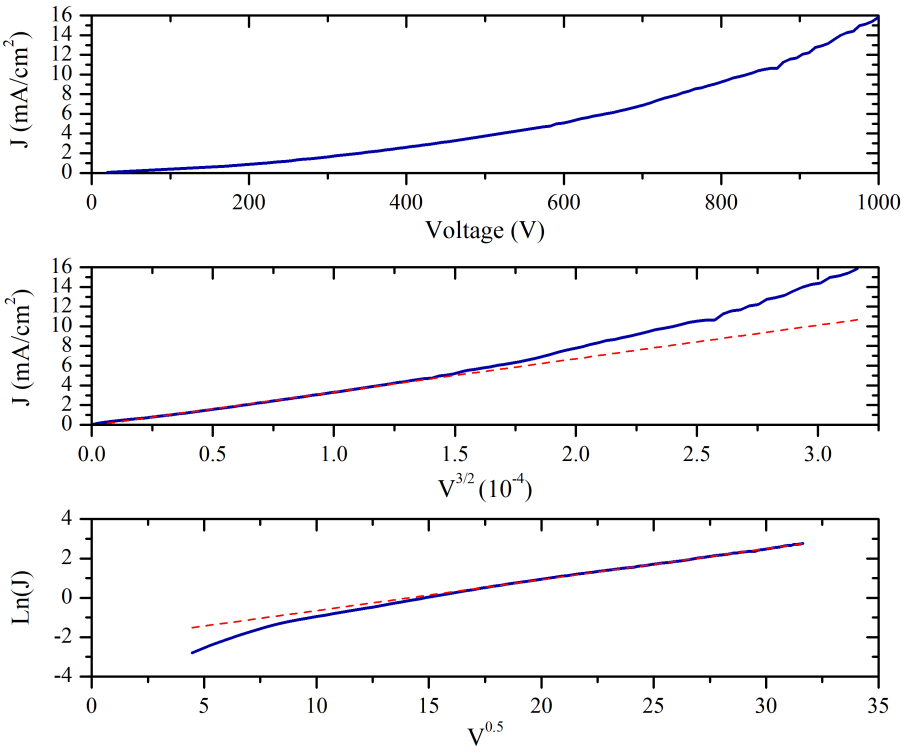


Fig. S 7. The bottom curve describes $\ln(J)$ against $V^{1/2}$. The dashed red lines correspond to a linear fitting. Data was obtained with a sintered LaB_6 disk heated to a temperature of 850 °C.

The gap between the emitting surface and the anode is governed by the space charge due to the electron flux in there. The maximum value of the electron current density is then given by the Child-Langmuir law:[27]

$$J = \frac{4\epsilon_0}{9}\sqrt{\frac{2e}{m_e}}\frac{V^{\frac{3}{2}}}{d^2} \tag{6}$$

As generally the distance d is kept constant, the electron current density is thus governed only by the potential difference V. At low electrical field E or low potential V, the delivered current intensity is limited by the electron space charge. It varies also as $V^{2/3}$. However at high E, or V, the space charge effect becomes negligible. The electron current is therefore governed only by the thermionic effect and it is given by equation (4). The extrapolation of the linear part of the curve $\ln(J) = f(\sqrt{V})$ gives the value of J_0 (current density in the absence of E field) that solely depends on the WF ϕ_0.

Mirror reflectivity calibration

The wavelength-dependence of the reflectivity of the mirrors, $R(\lambda)$ in Eq. (7), was established independently using the method described in Ref.[28] $R(\lambda)$ was determined based on the Rayleigh scattering cross-sections, α_{Ray}, of helium and carbon dioxide gases as described in Eq. (7):

$$\frac{1-R(\lambda)}{d} = \frac{(\frac{I_{CO_2}}{I_{He}})\alpha_{Ray}^{CO_2}(\lambda) - \alpha_{Ray}^{He}(\lambda)}{1-\frac{I_{CO_2}}{I_{He}}} \tag{7}$$

I_{CO_2} and I_{He} represent the light intensities transmitted by a cavity filled with 1 atm CO_2 or helium gas, respectively.

References

(1) Boufendi, L.; Bouchoule, A. Particle nucleation and growth in a low-temperature argon-silane discharge. *Plasma Sources Sci. Technol.* **1994**, *3*, 262–267.

(2) Boufendi, L.; Bouchoule, A.; Hbid, T. Electrical characterization and modeling of a dust forming plasma in a radio frequency discharge. *Journal of Vacuum Science & Technology A* **1996**, *14*, 572–576.

(3) Hollenstein, C.; Schwarzenbach, W.; Howling, A. A.; Courteille, C.; Dorier, J.; Sansonnens, L. Anionic clusters in dusty hydrocarbon and silane plasmas. *Journal of Vacuum Science & Technology A* **1996**, *14*, 535–539.

(4) Hanlon, P. From nanocrystals to DVD. *Nature Materials* **2005**, *4*, 878.

(5) Vach, H.; Brulin, Q. Controlled growth of silicon nanocrystals in a plasma reactor. *Phys. Rev. Lett.* **2005**, *95*, 165502.

(6) Chun, A. L.; Rodgers, P.; Segal, M.; Vaughan, O. Silicon nanocrystals: More is better. *Nature Nanotech* **2011**, *5*, 756.

(7) Rodgers, P. Briefings in Nanotechnology. *Scientific American* **2012**, *1*, 5.

(8) Vach, H. Ultrastable silicon nanocrystals due to electron delocalization. *Nano Lett.* **2011**, *11*, 5477–5481.

(9) Vach, H.; Ivanova, L. V.; Timerghazin, Q. K.; Jardali, F.; Le, H. L. T. Metallic-like bonding in plasma-born silicon nanocrystals for nanoscale bandgap engineering. *Nanoscale* **2016**, *8*, 18062–18069.

(10) Vach, H. Symmetric and irregular aromatic silicon nanoclusters. *Chem. Phys. Lett.* **2014**, *614*, 199–203.

(11) Gordeychuk, M. V.; Katin, K. P.; Grishakov, K. S.; Maslov, M. M. Silicon buckyballs versus prismanes: Influence of spatial confinement on the structural properties and optical spectra of the $Si_{18}H_{12}$ and $Si_{19}H_{12}$ clusters. *Int. J. Quantum Chem.* **2018**, *118*, e25609.

(12) Vach, H. Electron-deficiency aromaticity in silicon nanoclusters. *J. Chem. Theory Comput.* **2012**, *8*, 2088–2094.

(13) Vach, H. Terahertz and Gigahertz emission from an all-silicon nanocrystal. *Phys. Rev. Lett.* **2014**, *112*, 197401.

(14) Bleecker, K. D. Modeling of the formation and behavior of the nanoparticles in dusty plasma. Ph.D. thesis, University of Antwerpen, Belgium, 2006.

(15) Bouchoule, A.; Plain, A.; Boufendi, L.; Blondeau, J. P.; Laure, C. Particle generation and behavior in a silane-argon low-pressure discharge under continuous or pulsed radio-frequency excitation. *J. Appl. Phys.* **1991**, *70*, 1991–2000.

(16) Kresse, G.; Furthmüller, J. Efficiency of Ab Initio Total Energy Calculations for Metals and Semiconductors Using a Plane-Wave Basis Sets. *Comput. Mater. Sci.* **1996**, *6*, 15–50.

(17) Kresse, G.; Furthmüller, J. Efficient Iterative Schemes for Ab Initio Total-Energy Calculations Using a Plane-Wave Basis Sets. *Phys. Rev. B: Condens. Matter Mater. Phys.* **1996**, *54*, 11169–11186.

(18) Perdew, J. P.; Burke, K.; Ernzerhof, M. Generalized Gradient Approximation Made Simple. *Phys. Rev. Lett.* **1996**, *77*, 3865–3868.

(19) Grimme, S. Semiempirical GGA-Type Density Functional Constructed with a Long-Range Dispersion Correction. *J. Comput. Chem.* **2006**, *27*.

(20) Blöchl, P. E. Projector Augmented-Wave Method. *Phys. Rev. B: Condens. Matter Mater. Phys.* **1994**, *50*, 17953–17979.

(21) Windiks, B., R.; Delley Massive Thermostatting in Isothermal Density Functional Molecular Dynamics Simulations. *J. Chem. Phys.* **2003**, *119*.

(22) Nosé, S. A Unified Formulation of the Constant Temperature Molecular-Dynamics Methods. *J. Chem. Phys.* **1984**, *81*, 511–519.

(23) Richardson, O. W. Some Applications of the Electron Theory of Matter. *Phil. Mag.* **1912**, *23*, 594.

(24) Dushman, S. Electron Emission from Metals as a Function of Temperature. *Phys. Rev.* **1923**, *21*, 623.

(25) Pelletier, J.; Pomot, C. Work function of sintered lanthanum hexaboride. *Appl. Phys. Lett.* **1979**, *34*, 249–251.

(26) Dias, S.; Krupanidhi, S. B. Temperature dependent electrical behaviour of Cu_2SnS_3 films. *AIP Advances* **2014**, *4*, 037121.

(27) Lieberman, M. A.; Lichtenberg, A. J. *Discharge and Materials Processing Principles of Plasma Discharges and Materials*; Wiley Online Library, 2^{nd} edition: New York, 2005.

(28) Washenfelder, R. A.; Langford, A. O.; Fuchs, H.; Brown, S. S. Measurement of glyoxal using an incoherent broadband cavity enhanced absorption spectroscometer. *Atmos. Chem. Phys.* **2008**, *8*, 7779–7793.